Motion Artefact Suppression Method for Wearable ECGs

Huanqian Zhang and Jianlong Zhao

Abstract Due to the development of the Internet of Things, there has been increasing interest in the use of wearable electrocardiograms (WECGs) in the outdoor environment instead of in a resting state at a hospital. During daily activities, the WECG signals will suffer additional motion artefacts (MAs) originating from the interface between the electrode and the conductive adhesive and the stretching of the skin. However, MAs in WECG signals are highly difficult to suppress because MAs and WECG signals have similar frequency spectra.

In this review, we briefly discuss motion artefact suppression methods, from the origin of the motion artefacts to detecting the motion artefacts and then suppressing the motion artefacts.

The metabolic difference between the live skin cells of the inner layer and the dead skin cells of the stratum corneum create an 'injury current'. When a force is applied to the skin, the membrane of the dead skin cell breaks, and then, sodium will flow into the cells through the crack and ultimately form the 'injury current'. When the current flows through the resistor of the stratum corneum, there will be a potential change, which is the MA.

Adaptive filters (AFs) have been extensively applied in biomedical engineering because of their simplicity, real-time processing ability and robustness. These filters can remove MAs from WECG signals by using a reference signal that is correlated with MAs and uncorrelated with the WECG. We also describe two concepts of reference signal detection.

Because of the nonstationary properties of motion artefacts, low filter output distortion and high QRS beat detection accuracy cannot be simultaneously

H. Zhang (✉)
Chinese Academy of Science, Shanghai Institute of Microsystem and Information Technology, Shanghai, China
e-mail: henry.zhang@nus.edu.sg

J. Zhao (✉)
Chinese Academy of Science, Shanghai Institute of Microsystem and Information Technology, Shanghai, China
e-mail: jlzhao@mail.sim.ac.cn

C. Liu, J. Li (eds.), *Feature Engineering and Computational Intelligence in ECG Monitoring*, https://doi.org/10.1007/978-981-15-3824-7_5

generated. Hence, we propose a new feed forward combined adaptive filter algorithm to overcome this limitation.

Finally, we provide an overview of recent findings for the adaptive filter algorithm-based motion artefact suppression method.

Keywords Wearable ECG · Motion artefacts · Electrode tissue impedance · Noise suppression · Adaptive filter

1 Introduction

With the increase in human life expectancy, the trend of ageing is evident. In 2050, the population of elderly people (greater than 60 years old) will exceed that of young people (less than 15 years old). There will be a large expense in medical care because of ageing, and the health of elderly people will determine the overall cost of medical insurance and the frequency of using advanced medical equipment. Therefore, people must remain healthy as the life expectancy increases. Wearable medical services will be a major part of helping elderly people decrease the frequency of hospital medical treatments and increase their life expectancy.

Among the various medical conditions, heart disease has the highest mortality rate. ECGs are widely used to detect heart disease. Wearable ECGs are a new technology that extends ECG detection from hospitals to daily life. However, patients move about during the course of their daily life, and the weak ECG signal will be affected by motion artefacts, leading to an incorrect estimation of ECG features and triggering unnecessary warnings. Recently, many studies have been published to find the origins of motion artefacts and methods of suppressing motion artefacts.

In this chapter, we will review these studies. First, we will discuss the source of motion artefacts from the view of anatomical and circuit models. Second, we will describe the detection of motion artefacts from the electrical hardware system domain. Finally, we will introduce a method for suppressing motion artefacts using an adaptive filter.

2 The Origin of Motion Artefacts

Tam and Webster [1] found that the amplitude of the deformation potential decreases when the stratum corneum is scraped away. They concluded that the major source of motion artefacts is the skin/paste interface. The magnitude of the change in skin potential will be significantly affected by the degree of skin abrasion.

The skin is made up of three layers: the epidermis, the dermis and the subcutaneous layer. The stratum corneum is the surface layer, which is composed of dead cells. The stratum granulosum and the stratum basale are located below the surface layer, forming the layers of the epidermis. The dermis is located underneath the stratum basale. Connective tissue, elastic tissue and living cells make up the rest of the dermis.

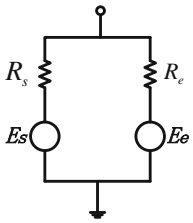

Fig. 1 Edelberg's skin model [1]

Many skin models have been suggested in the literature, but Edelberg's skin model is the most widely accepted.

In Fig. 1, E_e is the potential across the epidermis barrier membrane, wherein the magnitude of E_e is a function of the composition of the electrode paste. R_e is the total series resistance of the epidermis. Because $|E_e| < |E_s|$, skin abrasion decreases R_e such that $R_e \ll R_s$, thereby resulting in a less negative skin potential. Additionally, the smaller variation in R_e caused by skin deformation leads to a much smaller variation in skin potential.

E_s is the potential across the sweat duct membrane at the layer of the stratum basale. E_s is variable because of the diverse salt concentration in sweat. R_s is the total resistance in the sweat duct, for which the magnitude is determined by the height of the column of saline in the sweat duct and the permeability of the sweat duct wall. Sweat gland activity in response to sympathetic activation increases the sweat column, decreasing R_s. Hydration of the stratum corneum also has an effect on reducing R_e. The long settling time of the offset potential after applying the electrodes is the result of the wetting of the stratum corneum over time, which is caused by sweat and the interaction between the sweat and the paste. E_{skin} can be expressed as shown in Eq. (1):

$$E_{skin} = E_e + R_e\left(\frac{E_s - E_e}{R_s + R_e}\right) \tag{1}$$

A variation in the skin potential results from changes in any of the four parameters. Thus, the net variation in the offset potential of the recording system is the sum of the individual variations in skin potential under each electrode. Diagnostic ECG measurements usually use a lower cut-off frequency amplifier of 0.05 Hz. Very slow variations in the offset potential cause a negligible drift in the baseline. In contrast, rapid variations in the offset potential $(d_{E_{offset}}/d_{time})$ lead to obvious motion artefact problems. For example, when $d_{E_{offset}}/d_{time} = 2\,\text{mV}/\,\text{min}$, the baseline varies by 0.1 mV. The lower cut-off frequency is 0.5 Hz or higher in the monitoring mode, so that even greater variations in the offset potentials are tolerable.

The metabolic process of different skin layers causes ion diffusion [2].

Thakor and Webster [3] hypothesized that the metabolic process is the result of the differences in metabolic activity between the dead cells located in the outer layer of the skin and the cells located in the inner layer.

When mechanically stretching the skin, the skin potential V increases by several millivolts. Thakor and Webster explained the origin of this motion artefact ΔV as a reduction in the extracellular channel resistance Z.

The foundation of this model is based on two hypotheses. First, they hypothesized that the skin potential arises from a constant current source called 'injury current', which is generated by the difference in metabolic activity between the dead cells of the stratum corneum and the viable cells of the inner layers of the skin. Second, they hypothesized that this injury current flows through the extracellular channels, generating a negative DC voltage that drops from the inside to the outside of the skin. The skin potential is shown in Eq. (2):

$$V = (-R_{\mathrm{I}})(R_{\mathrm{m}})(I)/(R_{\mathrm{t}} + R_{\mathrm{C}} + R_{\mathrm{m}}) \tag{2}$$

where R_{C} is the impedance of the stratum corneum, R_{t} is the impedance of the transitional region shunted by the current I of negatively charged ions and $R_{\mathrm{m}}$is the impedance of the measuring device. With $R_{\mathrm{m}} \gg (R_{\mathrm{c}} + R_{\mathrm{t}})$, the following expression can be obtained:

$$V = (-R_{\mathrm{t}})(I) \tag{3}$$

Because of the first hypothesis (I is constant), the only way to obtain variations in V when stretching the skin is to assume that R_{t}alters $V : \Delta V = (-\Delta R_{\mathrm{t}})(I)$

In the report by Talhouet and Webster, their model is not perfect because of the values of ΔZ that can be positive or negative at high values of Z and the difference in shape between ΔV and ΔZ.

They explained the increase in Z in their study. They assumed that R_{c} increased more than R_{t} decreased when stretching the skin. The different behaviour between R_{c} and R_{t} could be clarified by the geometrical configuration of the skin cells. The decrease in R_{t} can be explained by the geometrical arrangement of the stratum basale and stratum granulosum, as stretching the skin causes the extracellular channels to increase in diameter. The stratum corneum cells fit together when they are displaced horizontally so that the horizontal channels between the cells form the main resistance pathway for ions.

When stretching the skin, the length of the current pathway increases, and the cross-sectional area of the current pathway decreases. This phenomenon occurs because the cells that are linked together by tight junctions or gap junctions can elongate under stretching.

They also suppose that the diffusion of Na+ ions across the proximal side of the membrane is increased by stretching a cell in the transitional layer. This action will cause the interior potential of the cell to be more positive. Viscoelastic stretching and relaxation of the cell membrane could occur with long time constants and cause variations in the skin potential with long time constants.

Burbank and Webster [4] studied the artefact potential amplitude and strain dependence as a function of the stretching force and time.

The skin under an electrode site was stretched for a time t with a repetition period r. A relationship was then defined between the resulting artefact potential amplitude A, which was defined as the maximum change in skin potential during skin stretching in relation to that just before skin stretching, and the relaxation time $(r - t)$ before stretching. The fitted equation appeared to be quite good, as shown in Eq. (4):

$$A = A_0\left(1 - e^{-(r-t)/\tau}\right) \tag{4}$$

where A_0 is the maximum artefact and τ is the time constant of the system. The time constant is 26 s, which is much longer than the electrical time constant of the skin at low frequencies, which is normally approximately 0.1 s.

By changing the stretching force and simultaneously monitoring the skin strain, potential and impedance, they compared the relationship between the strain and stretching force and the artefact potential. They increased the stretched mass from 0 to 1 kg and then decreased it again to 0 kg at a uniform rate of 30 g/s. The impedance was very nearly stable during this cycle. Although the strain was a nonlinear function of the stretched mass, it had a small time dependence or 'creep'. However, as discussed above, the artefact potential showed a very obvious time dependence.

3 The Detection of Motion Artefacts

Hamilton et al. [5] reported a system for evaluating and comparing motion artefact removal with sensors and impedance. A sinusoidal current was applied to an active electrode pair. They used the series resistances on the secondary side of the transformer to limit the current between the electrodes to 1 μA with a 1 V peak-to-peak output. Low-pass and high-pass filters were used to separate the impedance signal from the ECG and artefact signals. The low-pass filter and high-pass Butterworth filter had cut-off frequencies of 50 and 100 Hz, respectively. They applied an envelope detector to monitor the amplitude of the impedance signal after separating the motion artefact signal from the impedance signal. The final envelope signal was scaled to the impedance between the two electrodes. A bandpass filter with lower cut-off frequencies of 0.16 Hz and upper cut-off frequencies of 106 Hz removed the DC level of the impedance from the envelope signal. They converted the motion artefact signal to a digital signal with 10-bit resolution and a 120 Hz sample rate.

Spinelli et al. reported a simple direct method to measure the unbalance at power line frequency [6]. The external resistors R_c ensure a well-known common-mode input impedance. To apply the method to three electrode amplifiers, the third (right leg) electrode must be disconnected.

They measured actual skin-electrode impedances. Two plate electrodes (12 cm^2 in area) were placed on the right and left inner arms of the patient (ECG lead I). In the next experiment, they measured the imbalance in the electrode impedance between a

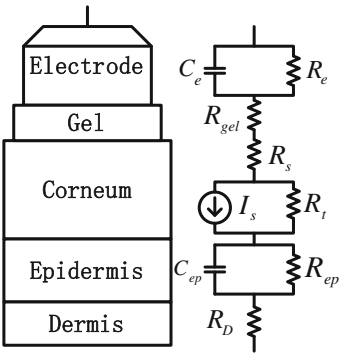

Fig. 2 Circuit representation of the skin-electrode interface and changes in electrical properties under motion artefacts [7]

plate electrode (right arm) and a cup electrode (left arm), which showed a significantly larger discrepancy than those obtained for two similar electrodes placed on the same location. The main interference voltage is expressed as shown in Eq. (5):

$$V_{\text{D.EMI}} = V_{\text{CM}} \frac{\Delta Z_{\text{E}}}{Z_{\text{C}}} \tag{5}$$

where ΔZ_{E} is the electrode-skin imbalance, Z_{C} is the average common-mode input impedance and V_{CM} is the patient common-mode voltage.

Romero et al. [7] reported an application-specific integrated circuit (ASIC) for monitoring three-lead ECG signals and one-channel skin-electrode impedance or electrode-tissue impedance (ETI). To calculate the ETI, they injected an AC signal and measured the voltage induced by the ETI. To avoid any interference with the ECG signal, the frequency of the AC signal needs to be outside the ECG range. They used a square-wave current at 2 kHz with a known amplitude. With the model shown in Fig. 2, concurrent measurement of the resistive and capacitive components was required for accurate measurement of the ETI information.

By demodulating the impedance signal with an in-phase frequency $f(0)$ and a quadrature-phase frequency $f(90)$, they separated the resistive and capacitive components.

The monitoring system synchronously measured the electrode-skin impedance and the ECG signal. The monitoring system comprised an instrumentation amplifier (IA), a ripple filter, a programmable gain amplifier and a bandwidth controllable low-pass filter. The injected AC signal modulates and measures the ETI. An instrumentation amplifier (IA) amplifies the resulting voltage and demodulates the voltage with in-phase and quadrature-phase chopper clocks. The output signal of the IA (in-phase, IMPI; quadrature-phase, IMPQ) will be filtered by a low-pass filter and amplified by a programmable gain amplifier (PGA) that has four different gains. The output signals are a measurement of the complex ETI.

The design of the current stimulation block should pay attention to the following two points. The first is the output impedance of the current generator, which may reduce the total input impedance of the ECG readout channel. The second is the DC

component of the AC source, which may further amplify the effect of motion artefacts at the output of the ECG channel. Therefore, they use a chopper-stabilized AC source. To set the mean value of the stimulation current to zero, they double the frequency of the AC signal to perform chopper stabilization. The continuous time impedance monitoring channels demodulate the resulting AC voltage over the electrode-skin interface. The ECG and impedance signals can be separated in the frequency domain with a low-pass filter.

Ottenbacher et al. [8] reported a method for detecting motion artefacts by the simultaneous measurement of electrode-skin impedance with an ECG signal. A sinusoidal current of 400 Hz was injected at the same electrodes between which the potential was measured.

High- and low-pass filters separated the impedance and potential signal, respectively. A dual lock-in amplifier reconstructed the impedance signal. They used a very small current of <1 μA to measure over a very wide range of electrode impedances (500 Ω to 1 MΩ) and avoid high filter orders to separate the ECG and impedance signal. They performed the experiments on the forearm of a test subject. They used tape to attach a fixed reference electrode with gel near the subject's elbow. In one experiment, they pressed (F_p) the dry measurement electrode against the subject's arm. In a second experiment, they stretched (F_s) the skin under the dry electrode while they pressed the electrode against the subject's arm with a small weight.

The results in their study showed that the force, potential and electrode-skin impedance depended on time (units: s). The potential is on the order of several mV, and the impedance decreases correspondingly when pressing the electrode against the subject's skin. When stretching the skin under the electrode, the potential exhibits an increase in the mV range, and the impedance also increases. The variation in the impedance is diverse from subject to subject and greatly relies on the humidity/sweat on the subject's skin. They assumed that the varying area of the electrode-skin contact, instead of the impedance change in the skin, leads to impedance changes. They also found a very good correlation between force, electrode impedance and electrode-skin potential. Nevertheless, it must be noted that actual movements are changing constantly with simultaneous stretching and pressing.

A measurement is made with two dry electrodes on the chest. The correlation between the impedance signal and the ECG signal against time is depicted. The amplitude of the peaks has less information because it depends on how large artefacts contaminate the signal. However, the peak reveals good correlation between the two signals.

Oberg [9] reported a method to monitor the skin-electrode contact. They added an AC voltage source with the potential U6 between the noninverting input of IC4 and the ground.

The ECG signal U_3 is independent of U_5 because of Eq. (6):

$$U_3 = (U_2 - U_1)\left(2 \cdot \frac{R_1}{R_2} + 1\right) \tag{6}$$

The feedback loop from the output to the inverting input passes all contact points A, B and C. Hereafter, assume that the impedances Z_a, Z_b and Z_c are no longer negligible and that the impedances Z_a and Z_b are equal. Z_t is the sum of the impedances between the ground electrode and one of the inputs, e.g. $Z_t = Z_a + Z_c$. A potential divider is formed by the impedance Z_t together with the input resistance R_{in} of the amplifier. In this case, the expression for U_5 will be Eq. (7):

$$U_5 = U_6\left|1 + \frac{2Z_t}{R_{\text{in}}}\right| \tag{7}$$

This means that U_5 is dependent on Z_t. If the ground electrode is completely loosened, i.e. $Z_t = \infty$, then U_5 goes to infinity. If the impedance $Z_a \neq Z_b$ by an amount Z_{diff}, then U_5 can be expressed as shown in Eq. (8):

$$U_5 = 2U_6\left|1 - \frac{1}{\frac{Z}{R_{\text{in}}} + 2}\right| \tag{8}$$

U_5 relies on the contact impedance. If one of the electrodes at points A or B becomes loose, Eq. (9) is obtained:

$$U_5 = 2U_6 \tag{9}$$

Hence, if we introduce a voltage source at the noninverting input of IC4, then the output voltage depends on the contact impedances Z_a, Z_b and Z_c. If we compare U_5 and U_6, we can decide whether the impedance in some of the contact points is too large.

Degen and Jackel [10] reported a new method that allows continuous monitoring of electrode-skin impedance. Each channel is preceded by a protection circuit, which limits the maximal current through the body to 50 μA. They applied the method to a three-electrode ECG without the additional reference electrode. The operations of the measurement circuit are explained hereafter. The driven right leg (DRL) loop will be forced by any voltage appearing at the positive input of the DRL op-amp. The system reacts in such a way that the differential input voltage of the DRL op-amp is again zero. In the case of a sinusoidal signal, this phenomenon occurs when the bandwidth of the DRL loop is larger than the signal frequency. Therefore, at the input of the instrumentation amplifier (INA), the sinusoidal voltage V_{add} appears as a common-mode voltage. The Common Mode Rejection Ratio (CMRR) of the INA rejects this additional common-mode voltage, except for the part converted to a differential signal by the electrode-skin impedance mismatch (potential divider effect) and amplified by the differential mode gain of each INA. This part is superimposed on the corresponding output voltage V_{outi}. If we exclude all other

signal sources, e.g. power line interference and bioelectric signals, the residual of the additional common-mode signal V_{addi} at electrode i can be calculated.

The input impedance mismatch is expressed in Eq. (10):

$$\Delta Z_{\text{el}} \Delta j\omega \overline{C_{\text{in}}} G_{\text{DM}} \approx \frac{V_{\text{addi}}}{V_{\text{add}}} \tag{10}$$

They applied a sinusoidal force to the signal electrode '*I*'. Moreover, they measured both the norm of the residual voltage |*V* _ addi| and the bioelectric recording. A strong relationship was found between the measured impedance mismatch and the baseline variation.

Bertrand et al. [11] reported that the prediction of motion artefacts at one electrode can be further improved by incorporating impedance measurements at other electrodes in EEG recording.

Comert and Hyttinen [12] reported a simultaneous measurement of impedance at eight current frequencies during the application of controlled motion to the electrode under the mounting force of the monitored electrode. They found that the motion is not reflected by the different frequencies of impedance measurements. The best correlation between impedance and the applied motion appeared when the impedance current frequencies were greater than 11 kHz. The impedance signal correlated well with the applied motion; however, impedance had a lower correlation to the actual motion artefact signal.

Zhang et al. [13] reported an approach that injects an additional common-mode signal through the reference electrode to simultaneously measure the electrode-tissue impedance and ECG signal. To suppress the MA in a WECG, a reference signal that has a high correlation with the MA and a low correlation with the WECG is required by an adaptive filter (AF). Figure 3 shows that the reference signal for the AF can be generated by the multichannel electrode-tissue impedance (MC-ETI) detection approach without any additional sensors.

A 1 kHz AC voltage is forced by amplifier A2 through the driven right leg circuit and electrode Z_{LA}. Two current paths flow through the body. One flows through Z_{LA}, Z_{RA}, and Z_{in} to the ground, and the other flows through Z_{LA}, Z_{LL}, and Z_{in} to the ground. The input impedance of the instrument amplifier is Z_{in}. LL is located several millimetres below the left breast, RA is located several millimetres below the right collarbone and LA is located several millimetres below the left collarbone.

When the electrode movement leads to the variation in Z_{LA}, Z_{LL}, and Z_{RA}, the divided voltages v_{LL} and v_{RA} will vary simultaneously. These voltages are differentially amplified by A3 and A4. A3 and A4 generate two AC voltages $v_{\text{ETI\_LL}}$ and $v_{\text{ETI\_RA}}$. Moreover, the WECG signal v_{ECG} is detected by A1. These voltages are sampled by an analogue-to-digital converter (ADC) with an 80 kHz sampling rate. The digital data are transported to the PC. The DC component from $v_{\text{ETI\_LL}}$ and $v_{\text{ETI\_RA}}$ is extracted by a digital lock-in amplifier. The MC-ETI signal can be calculated by Eqs. (11) and (12):

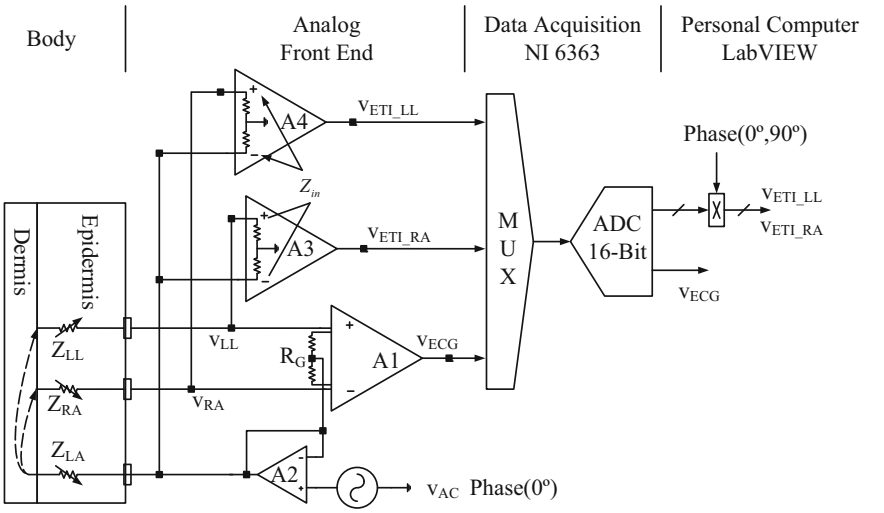

Fig. 3 MC-ETI detection approach [13]

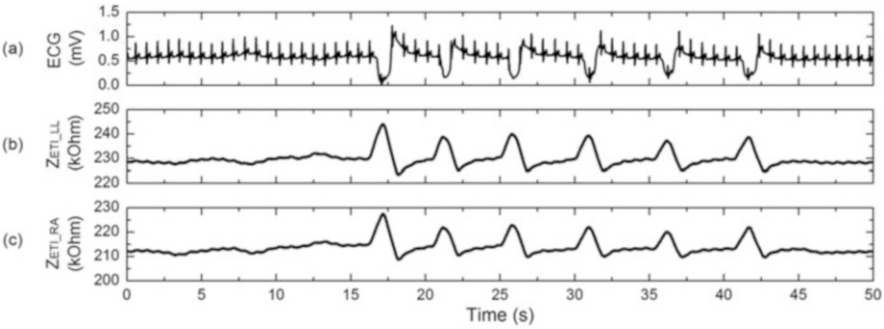

Fig. 4 (**a**) ECG signal and (**b**, **c**) MC-ETI signals [13]

$$Z_{\text{ETI\_LL}} \approx Z_{\text{LL}} \approx (Z_{\text{in}} - 2Z_{\text{LA}})V_{\text{ETI\_LL}}/2V_{\text{AC}} - 2Z_{\text{LA}} \tag{11}$$

$$Z_{\text{ETI\_RA}} \approx Z_{\text{RA}} \approx (Z_{\text{in}} - 2Z_{\text{LA}})V_{\text{ETI\_RA}}/2V_{\text{AC}} - 2Z_{\text{LA}} \tag{12}$$

The MC-ETI generating WECG and reference signals in the motionless and motion state with a period of 50 s are shown in Fig. 4. In the motion state (15–45 s), the WECG and MC-ETI signals have a high correlation. In the motionless state (0–15 and 45–50 s), these signals are stable but have low correlation.

The correlation between the MC-ETI and WECG signals over the time offset is shown in Fig. 5. There is no obvious peak in the black curve at zero time offset in the motionless state. However, in the motion state, the peak in the red curve at zero time offset shows a good correlation between these two signals.

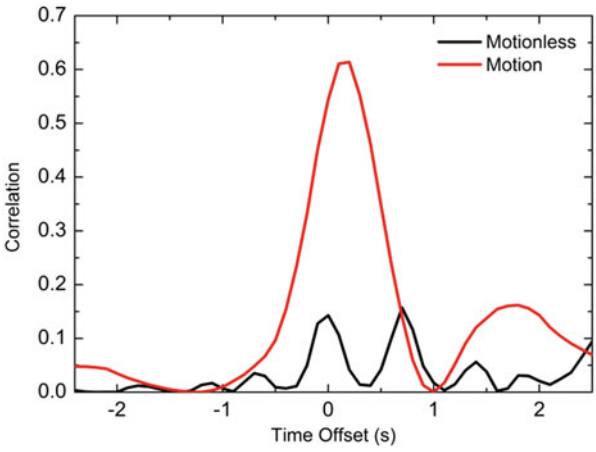

Fig. 5 Correlation as a function of the time offset [13]

4 Suppression of Motion Artefacts with an Adaptive Filter

With digital signal processing, the motion artefacts in ECG signals can be suppressed. Many studies have been reported on artefact suppression, which have mostly focused on two methods: blind source separation (BSS) and adaptive filtering.

Changli [14] reported that BSS has found many applications, including digital image processing, speech signal processing, medical signal processing, geophysical signal processing, communication signal processing and remote sensing image processing. When the mixing process and the original signals are unknown, BSS tries to decompose the observed sensor signals to obtain the unmixed source signals. However, given some assumptions, BSS has had great success, and many novel and effective methods have emerged.

Sweeney et al. [15] reported that, as a branch of BSS, independent component analysis (ICA) can separate different components from the source signals by defining them as statistically independent components.

Romero [16] reported that motion artefacts and ECG signals are statistically independent, so they can be separated by ICA.

However, ICA is restricted by data redundancy. ICA requires several independent sensors and cannot be used in one-channel sensor system, and it is necessary to ensure that the signal from each sensor is uncorrelated with other sensor signals. The large computational cost makes ICA very difficult to implement for real-time low-power applications.

The adaptive filter algorithm can automatically change its filter parameters and is widely used in the signal processing field.

Thakor and Zhu [17] reported that the adaptive filtering technique is useful in many biomedical applications. One simple but important application is in 60 Hz power line interference cancellation.

The adaptive filter has a low computational cost and high reliability, so it is very suitable for real-time low-power applications.

Tong et al. [18] reported that an adaptive filter using electrode motion as the reference signal can reduce motion artefacts. They measured electrode motion with two custom-developed sensors: anisotropic magnetoresistive (AMR) and accelerometer (ACC) sensors.

A two-axis AMR sensor was oriented parallel to the body surface, and a three-axis ACC sensor was developed using two dual-axis ACC chips.

Raya and Sison [19] reported using an accelerometer as a source of noise reference. Least mean squares (LMS) and recursive least squares (RLS) adaptive filter algorithms were used. They claimed that the major kinematic acceleration component during human movement is usually found in the vertical direction. Their adaptive filter can effectively reduce motion artefacts in stress ECGs.

Hamilton and Curley [20] reported that adaptive removal of motion artefacts can be 12.5 dB by using a skin stretching signal derived from sensors mounted on a foam electrode.

The most significant artefacts generated by skin stretching can still be adaptively removed. However, their sensors each cost approximately $600 because of the integrated stretching sensor.

Hamilton et al. [5] reported using a variable step size LMS (VSS-LMS) adaptive filter to remove motion artefacts in ECG signals:

$$\widehat{s}[n] = s[n] - \sum_{0}^{i} w_i n[n-i] \tag{13}$$

$$w_i^* = w_i + \beta \widehat{s}[n] \cdot n[n-i] \tag{14}$$

$$\beta[n] = \frac{a}{\sum_{i=1}^{200} \frac{|s[n-i] \cdot n[n-i]|}{200}} \tag{15}$$

where $s[n]$ represents the nth sample of ECG corrupted by noise, $n[n]$ represents the nth sample of the skin impedance or skin stretching signal and $\widehat{s}[n]$ is the nth estimation of the signal without motion artefacts. Note that 'w' represents filter coefficients that are iteratively updated after each sample by Eqs. (14) and (15), where 'a' is $8.44 \times 10^{-11}\ V^2$.

Wen-Ching et al. [21] reported using the normalized least mean squares (NLMS) adaptive filter algorithm to suppress the motion artefact from the primary input of ECGs. The 120-order finite impulse response (FIR) filter was adaptively adjusted by the NLMS with a 0.05 adaptive step size. They used the ACC signals and strain gauge (SG) signals as reference signals. They analysed the correlation between the ECG and ACC signals and the correlation between the ECG and SG signals. The higher one was chosen as the master reference, whereas the lower one was chosen as the slave reference.

Hyejung et al. [22] reported a two-stage cascade LMS adaptive filter for an ECG monitoring system. The first LMS stage consisted of analogue feedback, which

prevents signal saturation to reduce the input dynamic range. This approach employs a high-pass filter, which mainly targets the baseline wandering suppression to prevent signal saturation. An LMS algorithm with an adaptive step size is introduced and employed in the second LMS stage to remove the remaining motion artefact. The adaptive step size algorithm can achieve fast convergence to quickly track large sudden motion artefacts while preventing the distortion of the ECG component.

They reported a proposed LMS algorithm with adaptive step size control. The difference between their algorithm and the standard LMS algorithm is that they integrated an adaptive step size control block. The step size is updated to be large at a high signal-to-noise ratio (SNR) and small at a low SNR. The variation in both the reference signal $\sigma_{x(n)}$ and the input signal $\sigma_{d(n)}$ proportionally controls the step size adaptation function $\mu'(n)$, as shown in (16) and (17):

$$c(n) = \sigma_{x(n)} \cdot \sigma_{d(n)}/p \tag{16}$$

$$\mu'(n) = \begin{cases} \mu_0, 0 \le c(n) < \mu_0 \\ c(n), \mu_0 \le c(n) < 0.9 \\ 0.9, 0.9 \le c(n) \end{cases} \tag{17}$$

where 'σ' is the standard deviation (STD) of the signal during the half cycle of the heart rate and 'p' is the experimentally determined constant, which sets the $\mu'(n)$ range between 0 and 1.

Romero et al. [23] reported the performance of different implementations of adaptive filter (AF) algorithms in the context of motion artefact reduction in ECG signals.

They used the LMS algorithm with the accelerometer as a reference and recursive least squares (RLS), convex AF and LMS sign-error with the skin-electrode impedance (SEI) as a reference.

Zhang et al. [24] reported a feed forward combined adaptive filter (FFC-AF) which is consisted of two separate AFs (one fast convergence speed AF 'FCS-AF' and one high convergence accuracy AF 'HCA-AF') and one combination AF. The parameter combination varies with the estimation of the reference signal stationary. Figure 6 describes the structure of the FFC-AF, and the corresponding equation is shown in Eq. (18):

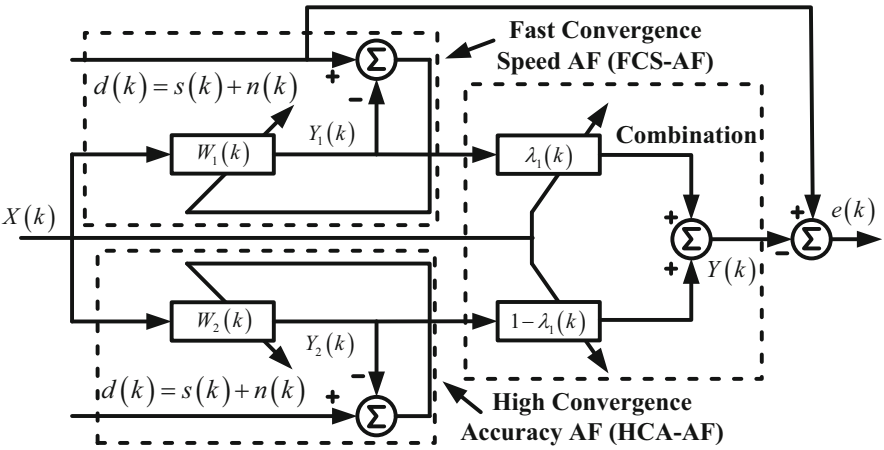

Fig. 6 FFC-AF block diagram [24]

$$\begin{cases} Y(k) = \lambda_1(k) \cdot Y_1(k) + [1 - \lambda_1(k)] \cdot Y_2(k) \\ Y_{1,2} = W_{1,2}^T(k) \cdot X(k) \\ \lambda_1(k) = \dfrac{2}{1 + \exp[-p \cdot \delta(k)]} - 1 \\ \delta(k) = \dfrac{1}{n} \sum\limits_{i=0}^{n-1} \left(x_i - \dfrac{1}{n} \sum\limits_{i=0}^{n-1} x_i \right)^2 \\ p = \begin{cases} p_{\text{non}} & \delta(k) \geq \delta_{\text{th}} \\ p_{\text{sta}} & \delta(k) < \delta_{\text{th}} \end{cases} \end{cases} \tag{18}$$

where $X(k)$ is the reference signal of two separate filters. Parameter $\lambda_1(k)$ is the combination weight of the filter output, which ranges between 0 and 1. At each iteration, $\lambda_1(k)$ updates its value according to the stationary degree of $X(k)$ by its variance $\delta(k)$. When $X(k)$ is in the stationary state, $\delta(k)$ is lower than the threshold δ_{th}, which means that AF is in the motion artefact (MA)-free state. Then, $\lambda_1(k)$ will remain at approximately 0 to increase the weight of the high convergence accuracy AF (HCA-AF) output. When $X(k)$ is in the nonstationary state, $\delta(k)$ is larger than δ_{th}, which means that AF is in the MA state. Then, $\lambda_1(k)$ will be maintained at approximately 1 to increase the weight of the fast convergence speed AF (FCS-AF) output.

Figure 7 shows the AF results, in which one triangle represents one QRS beat detection.

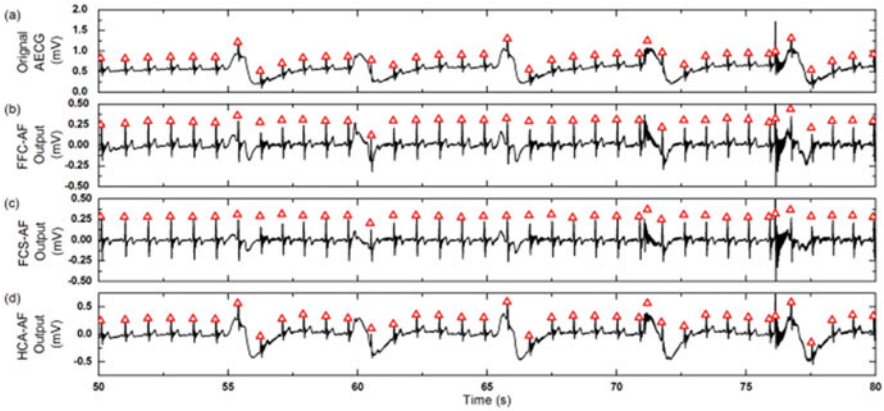

Fig. 7 Adaptive filter results and QRS beat detection [24]

5 Conclusion

With the development of wearable medical technology, an increasing number of patients with wearable healthcare monitoring devices are moving home from the hospital. ECGs are important vital tests, which are the basis of wearable healthcare monitoring.

This chapter illustrates the origins of motion artefacts in ECG signals. Interesting experimental results are introduced to describe the physical reasons for the observed motion artefacts. Moreover, circuit models are provided to qualitatively explain the motion artefacts. Then, we describe the detection of motion artefacts. Several electrical circuit architectures are provided from single-channel skin-electrode impedance measurements and multichannel skin-electrode impedance measurements. Finally, we summarize the application of an adaptive filter in motion artefact suppression. The LMS, NLMS, VSS-LMS, cascade LMS and FFC LMS algorithms are discussed. These algorithms form the foundation for developing an ECG system without motion artefacts.

References

1. Tam, H., Webster, J.G.: Minimizing electrode motion artifact by skin abrasion. IEEE Trans. Biomed. Eng. **BME-24**(2), 134–139 (1977)
2. Talhouet, H., Webster, J.G.: The origin of skin-stretch-caused motion artifacts under electrodes. Physiol. Meas. **17**(2), 81–93 (1996)
3. Thakor, N., Webster, J.: The origin of skin potential and its variations. Proc. Ann. Conf. Eng. Biol. Med. **20**, 212 (1978)
4. Burbank, D.P., Webster, J.G.: Reducing skin potential motion artifact by skin abrasion. Med. Biol. Eng. Comput. **16**(1), 31–38 (1978)

5. Hamilton, P. S., et al.: Comparison of methods for adaptive removal of motion artifact. In: Computing in Cardioliology, vol. 27, pp. 383–386 (2000)
6. Spinelli, E.M., et al.: A practical approach to electrode-skin impedance unbalance measurement. IEEE Trans. Biomed. Eng. **53**(7), 1451–1453 (2006)
7. Romero, I., et al.: Motion artifact reduction in ambulatory ECG monitoring: an integrated system approach. In: Proceedings of the 2nd Conference on Wireless Health, San Diego, California, 2011 (2011)
8. Ottenbacher, J., et al.: ECG electrodes for a context-aware cardiac permanent monitoring system. In: Magjarevic, R., Nagel, J.H. (eds.) World Congress on Medical Physics and Biomedical Engineering 2006, vol. 14, pp. 672–675. Springer, Berlin (2007)
9. Oberg, T.: A circuit for contact monitoring in electrocardiography. IEEE Trans. Biomed. Eng. **BME-29**(5), 361–364 (1982)
10. Degen, T., Jackel, H.: Continuous monitoring of electrode skin impedance mismatch during bioelectric recordings. IEEE Trans. Biomed. Eng. **55**(6), 1711–1715 (2008)
11. Bertrand, A., et al.: Motion artifact reduction in EEG recordings using multi-channel contact impedance measurements. In: Biomedical Circuits and Systems Conference (BioCAS), pp. 258–261 (2013)
12. Comert, A., Hyttinen, J.: Impedance spectroscopy of changes in skin-electrode impedance induced by motion. Biomed. Eng. Online. **13**, 149 (2014)
13. Zhang, H., et al.: A multi-channel electrode tissue impedance detection approach for motion artifact suppression in ambulatory electrocardiography. In: Computing in Cardiology Conference (CinC), pp. 117–120 (2015)
14. Changli, L.: Study on Some Algorithms for Blind Source Separation and Their Applications. Xidian University, Xian (2010)
15. Sweeney, K.T., et al.: Artifact removal in physiological signals—practices and possibilities. IEEE Trans. Inf. Technol. Biomed. **16**(3), 488–500 (2012)
16. Romero, I.: PCA and ICA applied to noise reduction in multi-lead ECG. In: Computing in Cardiology, pp. 613–616 (2011)
17. Thakor, N.V., Zhu, Y.-S.: Applications of adaptive filtering to ECG analysis: noise cancellation and arrhythmia detection. IEEE Trans. Biomed. Eng. **38**(8), 785–794 (1991)
18. Tong, D., et al.: Adaptive reduction of motion artifact in the electrocardiogram. In: 24th Annual Conference and the Annual Fall Meeting of the Biomedical Engineering Society EMBS/BMES Conference, vol. 2, pp. 1403–1404. IEEE (2002)
19. Raya, M.A.D., Sison, L.G.: Adaptive noise cancelling of motion artifact in stress ECG signals using accelerometer. Eng. Med. Biol. **2**, 1756–1757 (2002)
20. Hamilton, P.S., Curley, M.G.: Adaptive removal of motion artifact. IEEE Eng. Med. Biol. Soc. **1**, 297–299 (1997)
21. Wen-Ching, L., et al.: Adaptive reduction of motion artifact in a portable ECG system. Sensors. 704–707 (2010)
22. Hyejung, K., et al.: Motion artifact removal using cascade adaptive filtering for ambulatory ECG monitoring system. In: Biomedical Circuits and Systems Conference (BioCAS), pp. 160–163 (2012)
23. Romero, I., et al.: Adaptive filtering in ECG denoising: a comparative study. In: Computing in Cardiology (CinC), 2012, pp. 45–48 (2012)
24. Zhang, H., et al.: Motion artifact suppression in ambulatory ECG with feed forward combined adaptive filter. In: 2016 Computing in Cardiology Conference (CinC). IEEE (2016)